The Role of Internal Gravity Waves in the Equatorial Current System

ERIC D. SKYLLINGSTAD AND DONALD W. DENBO

Battelle/Marine Sciences Laboratory, Sequim, Washington

(Manuscript received 17 November 1992, in final form 17 February 1994)

ABSTRACT

Using a two-dimensional nonhydrostatic model, experiments were performed to investigate the formation and maintenance of internal waves in the equatorial Pacific Ocean. The simulations show that internal waves are generated in the surface mixed layer by a type of Kelvin–Helmholtz instability that is dependent on both the flow Reynolds number (i.e., shear strength) and Richardson number. Because of the Richardson number dependence, the simulated internal waves exhibit a diurnal cycle, following the daily stability change in the mixed layer. The diurnal cycle is not evident when the wind stress is eastward because of a decreased mixed layer shear and corresponding Reynolds number. The amplitude, wavelength, frequency, and diurnal variability of the simulated waves are in agreement with high-resolution thermistor chain measurements. Linear theory shows that the horizontal wavelength of the internal waves depends on both the thermocline stratification and the strength of the Equatorial Undercurrent.

The simulations show that internal waves can provide an efficient mechanism for the vertical transport of horizontal momentum. In the surface mixed layer, the internal waves gain westerly momentum at the expense of the background flow. In some cases, this momentum is transferred back to the mean flow at a critical level resulting in a deceleration below the undercurrent core. Otherwise, the waves tend to decrease the current velocity above the undercurrent core.

1. Introduction

Finescale measurements of the vertical structure in the equatorial Pacific reveal a complex system of turbulence and wavelike motions in the shear zone above the Equatorial Undercurrent (EUC). These disturbances often exhibit a diurnal variation as shown by measurements of turbulent dissipation rates. Wijesekera and Dillon (1991) attributed this behavior to unstable, internal gravity waves that overturn and form turbulence just below the surface mixed layer. McPhaden and Peters (1992) present time series data from three separate experiments that support the linkage between internal waves and high dissipation rates. They show that a diurnal cycle exists not only in the turbulence but also in the variance of temperature and vertical displacement (i.e., internal wave field), indicating a dynamic link between strong internal waves and high turbulent dissipation rates. These results are corroborated by Moum et al. (1992) using towed thermistor chain data along the equator from about 140°W to 125°W during April 1987. They observed a strong diurnal cycle in the spectrum of vertical isotherm displacement with a peak amplitude at wavelengths between 100 and 250 m. The waves were observed at night and in the early morning hours during westerly wind events. Again, the wave observations were coincident with high turbulent dissipation rates. A companion paper by Hebert et al. (1992) examined the detailed structure of a single overturning wave event as shown in Fig. 1. Turbulent dissipation rates for this case were three orders of magnitude greater than background values, providing direct evidence that breaking internal waves cause increased turbulence.

Many authors have suggested that internal waves, in addition to causing turbulence below the mixed layer, can vertically transport zonal momentum in the equatorial ocean. For example, Dillon et al. (1989) found that during the 1984 Tropic Heat I Experiment, the turbulence stress divergence, calculated from turbulence dissipation rate measurements, did not balance the pressure and horizontal advection terms in the momentum equation. The imbalance was particularly large above 30 m and below 60 m. More recently, Hebert et al. (1991) performed a similar calculation using the 1987 field data and found significant momentum imbalances below 40 m. Wijesekera and Dillon (1991) proposed that westward moving internal waves, generated by convective plumes, were responsible for the missing momentum flux. In their conceptual model, internal waves forced at the base of the mixed layer reduce the easterly background flow above the undercurrent core through turbulence brought on by Kelvin–Helmholtz instability. Beneath the turbulent layer, they suggested that the internal waves transport westerly momentum to depths well

Corresponding author address: Dr. E. Skyllingstad, Battelle/Marine Sciences Laboratory, Sequim, WA 98382.

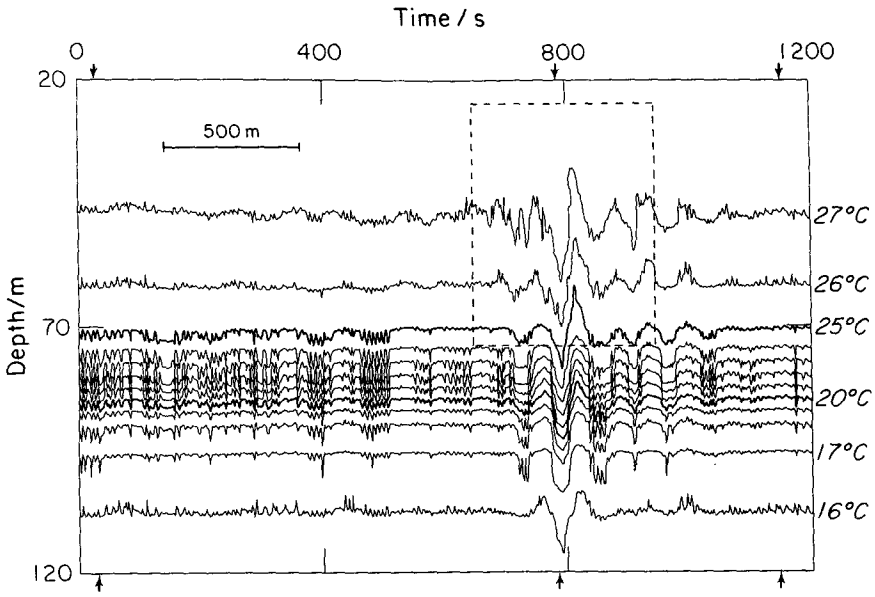

FIG. 1. Thermistor-chain temperature data taken over a 20-min period starting at 1634 UTC 16 April 1987 (from Hebert et al. 1992).

below the undercurrent core explaining the missing momentum flux.

Observational studies have revealed details of small-scale internal waves in the equatorial ocean, but only on specific dates and with limited space and time resolution. Consequently, it is not possible to determine from observations alone the importance of internal waves in the vertical transfer of momentum and heat. Also, observations have not provided a detailed analysis showing how the internal waves are formed. These questions have motivated us to design a numerical experiment to simulate equatorial internal waves and study their effect on the equatorial current system. Among the parameters that need to be explored are basic internal wave characteristics such as the phase speed and vertical wavenumber. Also, a better understanding of the instability process leading to internal wave formation is needed to properly represent internal waves in large-scale models of the equatorial oceans.

We address these problems in this study by applying a two-dimensional, nonhydrostatic model to a zonal cross section of the equatorial ocean. In contrast to large-scale equatorial modeling studies (e.g., Moore and Philander 1978), a nonhydrostatic model was required here because of the small-scale structure of the observed internal waves that we planned to simulate. According to Gill (1982, chapter 6), the hydrostatic assumption is only applicable for internal waves if $k \ll N/U$, where k is the horizontal wavenumber, N is the Brunt–Väisälä frequency, and U is the mean zonal current speed. Substitution of appropriate values for these parameters from the case shown in Fig. 1 (i.e., $k = 0.025$ m^{-1}; $N = 0.01$ s^{-1}; $U = 0.5$ m s^{-1}) shows that the scale of the internal waves is too small for a hydrostatic representation.

One of the main goals of this research was to develop a consistent, conceptual model of the internal wave formation process. Our numerical experiments show that internal waves are forced by a type of Kelvin–Helmholtz instability produced when a mixed layer has both strong shear (or high Reynolds number) and a Richardson number near 0. Because the daily heating cycle causes a variation in the mixed layer Richardson number value, internal wave activity undergoes a diurnal cycle with the wave intensity reaching a maximum just before sunrise. The observed sensitivity of internal wave formation to the surface wind stress direction can be explained in terms of the reduced mixed layer shear. In the simulations, east winds promote strong mixed layer current shear, low Richardson numbers, and a strong wave diurnal cycle, while west winds lead to weak shear in the mixed layer, higher Richardson numbers, and reduced internal wave activity.

We also examined the effect of internal waves on the momentum budget of the EUC. The EUC is forced as part of a balance between the basin-scale eastward directed pressure gradient and the westward directed surface wind stress. A key part of this balance is the transfer of westward momentum from the surface to the undercurrent core (Bryden and Brady 1985). We found that internal waves generated in the simulations always have a propagation direction that is westward relative to the undercurrent and therefore can transport westward momentum. The simulated wave momentum transport is comparable to bulk estimates of large-scale fluxes given in Hebert et al. (1991) and Dillon et

al. (1989), indicating that internal waves can be a significant process in the zonal momentum budget of the equatorial currents. Our results also show that a critical layer can exist below the undercurrent in cases where the surface mixed layer zonal velocity matches the velocity beneath the undercurrent core. In these cases, westward momentum is directly transported below the undercurrent and transferred to the mean flow at the critical layer. This result could have implications for future observation strategies for instrumentation below the undercurrent core.

A description of the numerical model and the model initial and boundary conditions is presented in section 2. Section 3 presents results from experiments using observed temperature profiles from April 1987, November 1984, and May–June 1987. The paper is concluded in section 4 with a discussion and summary of the model results.

2. Model description

We chose a 2D model for our experiments so that high-resolution comparison cases could be economically calculated. Clearly, two-dimensional results cannot fully substitute for a 3D simulation, particularly when internal wave overturning may be active (Winters and Riley 1992). However, for internal waves Hauf and Clark (1989) found in their modeling experiments that the 2D wave scale and sensitivity to shear and stability were similar to the 3D solution. Our analysis concentrates on the internal wave characteristics up to the point where the waves begin to break. The simulations show that wave breaking is not active when the internal waves are initially forming and, in general, affects the waves only after they reach a significant amplitude.

a. Model equations

The model equations are similar to those used in the large eddy simulation model presented by Deardorff (1980), with the major difference being the simplified subgrid-scale parameterization used here. The momentum equations are

$$\frac{\partial u}{\partial t} = -u\frac{\partial u}{\partial x} - w\frac{\partial u}{\partial z} - \frac{\partial P}{\partial x} - \frac{\partial}{\partial x}(\overline{u''^2}) - \frac{\partial}{\partial z}\overline{(u''w'')}, \tag{1}$$

$$\frac{\partial w}{\partial t} = -u\frac{\partial w}{\partial x} - w\frac{\partial w}{\partial z} - \frac{\partial P}{\partial z} - g\frac{\rho'}{\rho_0} - \frac{\partial}{\partial x}(\overline{u''w''}) - \frac{\partial}{\partial z}(\overline{w''^2}) - \left\langle -u\frac{\partial w}{\partial x} - w\frac{\partial w}{\partial z} - g\frac{\rho'}{\rho_0} - \frac{\partial}{\partial x}(\overline{u''w''}) - \frac{\partial}{\partial z}(\overline{w''^2})\right\rangle \tag{2}$$

and

$$\frac{\partial u}{\partial x} + \frac{\partial w}{\partial z} = 0, \tag{3}$$

where

$$P = \frac{p}{\rho_0}, \tag{4}$$

u and w are the zonal and vertical velocity components, respectively, p is the perturbation pressure, double-prime variables represent subgrid-scale motions, and the angle brackets denote a horizontal mean. Following Deardorff (1980) and Moeng (1984), the mean tendency for the vertical motion is subtracted from the vertical momentum equation to ensure that the horizontally averaged w and P remain equal to zero. This averaging is equivalent to removing hydrostatic changes in the total pressure that result from bulk increases or decreases in the temperature. The full density is calculated as

$$\rho = \rho(T, s, p), \tag{5}$$

where T, s, and p are temperature, salinity, and pressure, respectively. This function is calculated using the IES 80 equation of state as documented in UNESCO (1981). Components of the full density are defined as

$$\rho = \bar{\rho}(z) + \rho', \tag{6}$$

where

$$\bar{\rho}(z) = \frac{1}{L_x}\int_0^{L_x} \rho|_{t=0}\, dx. \tag{7}$$

Here ρ' is the resolved perturbation density; L_x, L_z are the horizontal and vertical domain size. For all momentum terms except for buoyancy, a constant density defined as

$$\rho_0 = \frac{1}{L_x L_z}\int_0^{L_x}\int_0^{L_z} \rho|_{t=0}\, dx dz \tag{8}$$

is used. Pressure is solved diagnostically using

$$\nabla^2 P = \left(\frac{\partial}{\partial x}(R_u) + \frac{\partial}{\partial z}(R_w + \langle R_w\rangle)\right), \tag{9}$$

where R_u and R_w are the right-hand sides (except for the P gradient terms) in Eqs. (1) and (2). The transport of temperature, T, is governed by

$$\frac{\partial T}{\partial t} = -u\frac{\partial T}{\partial x} - w\frac{\partial T}{\partial z} - \frac{\partial}{\partial x}(u''T'') - \frac{\partial}{\partial z}(w''T''). \tag{10}$$

The subgrid-scale turbulence parameterization follows the method of Smagorinsky (1963), where

$$\overline{u_i'' u_j''} = -K_m\left(\frac{\partial u_i}{\partial x_j} + \frac{\partial u_j}{\partial x_i}\right) \tag{11}$$

and

$$\overline{u_i'' \phi''} = -K_h \frac{\partial \phi}{\partial x_i}, \tag{12}$$

with ϕ denoting scalar quantities such as salinity or temperature. For the turbulence closure, we chose the local scheme described by Lilly (1962) where the eddy coefficients are defined as

$$K_m = K_h = (0.5\Delta)^2 |\mathrm{def}(1 - \mathrm{Ri}_t)^{1/2}, \tag{13}$$

with the turbulence closure Richardson number

$$\mathrm{Ri}_t = -\frac{g}{\rho}\frac{\partial \rho}{\partial z} \Big/ \mathrm{def}^2 \tag{14}$$

and

$$\mathrm{def}^2 = \left(\frac{\partial u}{\partial x} - \frac{\partial w}{\partial z}\right)^2 + \left(\frac{\partial u}{\partial z} + \frac{\partial w}{\partial x}\right)^2, \tag{15}$$

where Δ is equal to the grid spacing. When the Ri_t is greater than 0, the eddy coefficients are set to background values that are equal to the molecular diffusion.

The model equations of motion are solved using a centered-in-time, centered-in-space differencing scheme, while scalar advections use a hybrid scheme based on Colella (1990) with a monotonicity constraint as described by van Leer (1977) and Allen et al. (1991). Model grid spacings of 5 m and 2.5 m were used with time steps of 2.5 and 1.25 s, respectively, accounting for the fastest possible internal wave mode. The low-resolution grid spacing was used in all but one of the simulations reported. To reduce the amplitude of small-scale numerical instabilities, a ∇^{12} filter operator was applied at each model time step to the u and w fields. This filter has minimal effect on motions that are greater than 3 gridpoint spacings. Also, the filter is multiplied by a factor of 0.0025, which limits the degree of smoothing even more. The use of the filter on the momentum terms ensures that nonlinear numerical instability or aliasing is minimized in regions where the turbulence parameterization is not active because of strong stratification (Klemp and Wilhelmson 1978).

b. *Boundary conditions and large-scale forcing*

At the model top, a surface heat flux was imposed using an idealized diurnal heating cycle following the observations of Moum et al. (1989) and Hebert et al. (1991) (Fig. 2). Wind stress, τ, was prescribed by replacing the surface eddy diffusion term with

$$K_m \frac{\partial u}{\partial z}\bigg|_{sfc} = \frac{\tau}{\rho_0}. \tag{16}$$

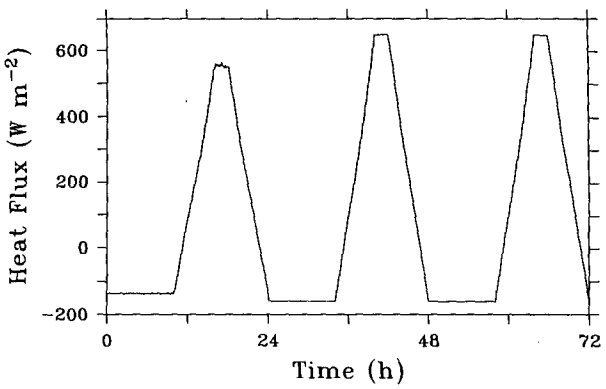

FIG. 2. Surface heat flux applied to the model surface. The diurnal cycle is an approximation of measurements reported in Moum et al. (1989).

We used a rigid-lid approximation ($w \equiv 0$) at the model top and calculated the boundary pressure gradient using Eq. (2) with the local acceleration or left-hand side set equal to zero.

At the model bottom, constant gradient conditions for temperature and zero gradient conditions for w and u were applied. A radiation boundary condition for pressure from Klemp and Durran (1983) was used to prevent internal wave reflection from the model bottom. For the lateral boundaries, periodic conditions were applied with the assumption that the scale of the internal waves was at least 3 to 4 times smaller than the model domain size. While this approach was convenient and produced reasonable results, it did affect the wavelengths of internal waves generated by the model, as discussed in the results section.

c. *Initial conditions*

The model initial conditions were determined by linearly interpolating observed temperature and velocity profiles to the model gridpoint locations. For each profile, missing data, such as the upper 15 m of the observed velocity profiles, were initialized by linearly extrapolating known data to the model grid points. Because data were typically not available below about 150 m, the profiles were linearly extended downward assuming values of temperature and velocity similar to those presented in Bryden and Brady (1985). Moum et al. (1989) show that temperature has a much greater influence than salinity on the vertical density structure in the equatorial Pacific. Therefore, the salinity was assumed constant for the cases simulated here. Also, to simplify the 2D assumption, we did not include a north–south component of velocity. Simulations were started with uniform horizontal conditions. Spatially and temporally random fluctuations of the heat flux, up to 30% of the prescribed value, were applied during the first day to facilitate spinup of the resolved model eddies (Fig. 2).

3. Results

Four primary numerical experiments were performed starting with a general simulation designed to reveal the processes governing the internal wave diurnal cycle, structure, and evolution. The next experiment addressed the importance of the ambient temperature and velocity profiles on the resulting scale of the internal waves. This was followed by an experiment where we examined the role of the horizontal current profile in determining the vertical transfer of horizontal momentum by the internal waves. Finally, an experiment was performed to determine the importance of surface wind stress direction on internal wave formation.

Initialization for the first experiment was taken from conductivity–temperature–depth data reported in Hebert et al. (1991) from 0630 UTC 17 April 1987. These data were measured on the equator near 134°W during a transect from 140° to 110°W. This case was selected for the basic simulation because of concurrent, high temporal resolution (20 Hz) thermistor-chain measurements, which show strong evidence of internal wave activity. Of particular interest was the observation of a significant peak in the wavenumber spectrum for disturbances with wavelengths of about 250 m. These features also displayed a significant diurnal cycle and a strong sensitivity to the direction of the surface wind stress (Moum et al. 1992). Profiles of temperature and zonal velocity for this case (Fig. 3, labeled 134W-1987) show a typical equatorial thermocline structure with a relatively weak, bimodal undercurrent core. The zonal current strength was unusually weak for the months of April and May when the undercurrent is normally at a maximum with a velocity between 1.0 and 1.5 m s^{-1} (McPhaden and Taft 1988). A diurnal cycle in the turbulence dissipation rate was evident in the low Richardson number region that extended from the surface to about 40 m in depth. Wind stress during this field experiment varied from about -0.05 N m^{-2} to 0.01 N m^{-2}.

a. Diurnal cycle

The wind stress for the first simulation was set to a constant value of -0.025 N m^{-2}, approximating wind stress observations during the first part of the 1987 field experiment, when internal waves were present. A domain size of 1280 m by 300 m was used with a grid size of 256 points in the horizontal by 60 points in the vertical and a grid spacing of 5 m. The model was run for 3 days beginning at sunset or the start of the convective period (see Fig. 2). Results showing the horizontally averaged values of temperature and absolute value of vertical velocity or wave intensity are shown as a function of time in Fig. 4. With the exception of the initial 12-h spinup period, the model simulates a diurnal cycle in both the thermodynamic and velocity fields during the 3-day period. In general, on each day the wave kinetic energy increases as indicated by the absolute value of the vertical motion, with some variability, to a maximum near sunrise and decreases throughout the heating period. A similar cycle is noted in the surface mixed layer where the vertical temperature field is uniform during the nighttime cooling period and stratified during the daytime heating.

The change in heat flux or temperature at the model top drives the mixed layer daily cycle, as shown by the variation in the temperature between the surface and 30-m depth during the 3-day simulation. The diurnal

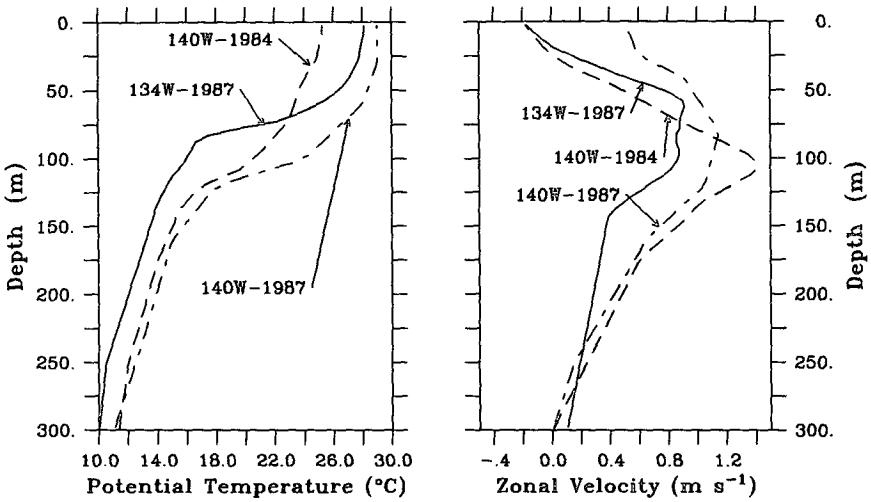

FIG. 3. Initial profiles of potential temperature and zonal velocity at 0630 UTC 17 April 1987 taken near 134°W on the equator (134W-1987), at 0230 UTC 28 November 1984 taken near 140°W on the equator (140W-1984), and average data from 12 May–11 June 1987 at 140°W (140W-1987). Eastward zonal velocity is positive and westward zonal velocity is negative.

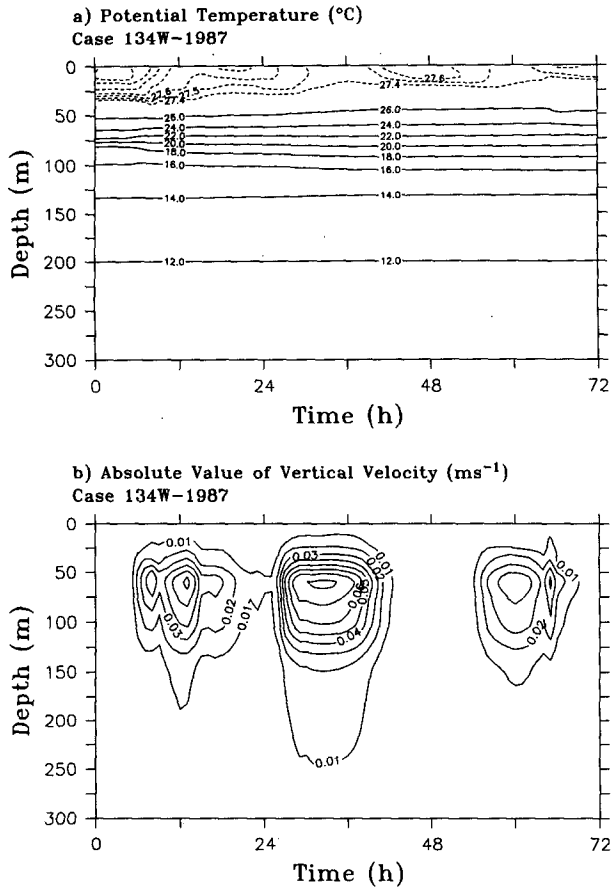

FIG. 4. Simulated horizontally averaged (a) potential temperature and (b) absolute value of vertical velocity as a function of time and depth for the 134W-1987 case. The contour interval for potential temperature is 2°C, with contours greater than 27.4°C plotted every 0.1°C (dashed). The contour interval for vertical velocity is 0.01 m s^{-1}.

temperature cycle at 2.5 m is of the same order (~0.2°C) as observations taken along the equator (Moum et al. 1989). The mixed layer depth, as indicated by a uniform surface temperature, increases from about 10 m during the day to about 25 m at night, agreeing with the daily range presented Moum et al. (1992). In addition to the short-term, diurnal variability, Fig. 4 also shows long-term changes in the mean temperature. These trends are brought on by the cumulative effects of the limited domain size and the 2D model framework. The effects of the profile changes are the likely cause of the internal wave variability apparent between each simulation day. For example, the strength of the maximum internal wave activity as shown by the absolute value of the vertical velocity differs between days 2 and 3 with the latter showing much weaker internal wave activity but with a secondary peak after sunrise on day 3. These day-to-day variations in internal wave activity are comparable to observed variability as demonstrated by measurements of temperature presented in Moum et al. (1992) and McPhaden and Peters (1992). As a consequence, we do not believe that the long-term trends have a significant impact on the internal wave dynamics that are of interest here.

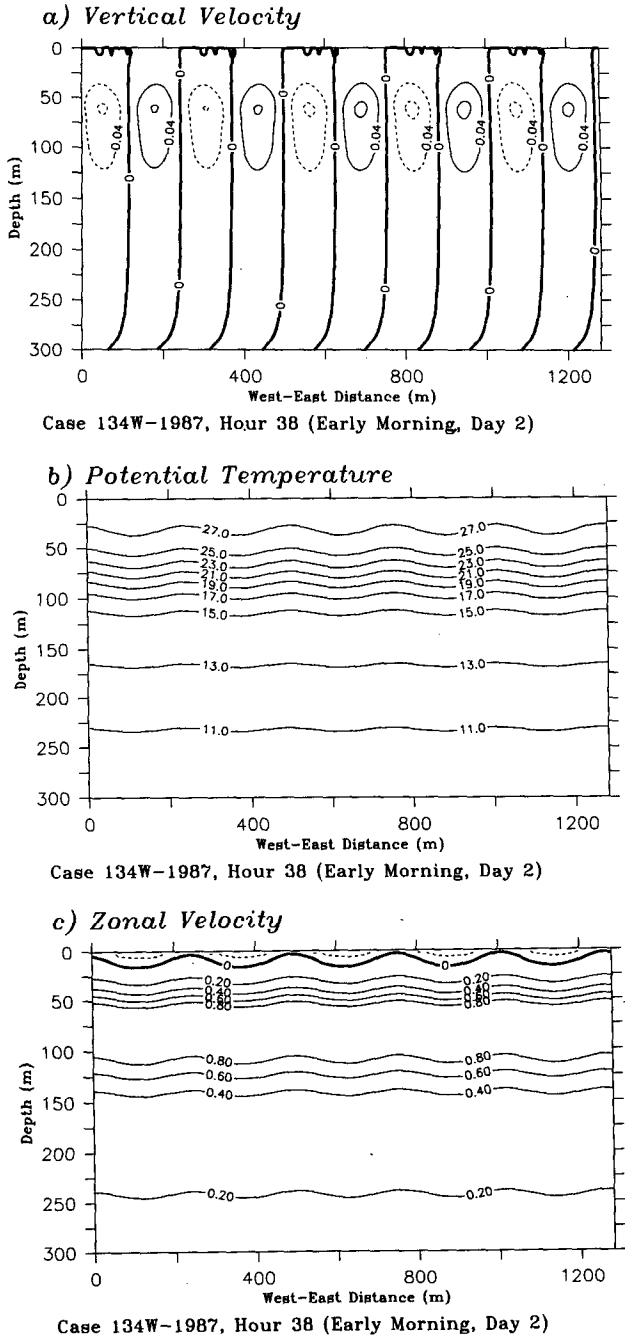

FIG. 5. Vertical velocity (a), potential temperature (b), and zonal velocity (c) for hour 38 from the 134W-1987 case as a function of depth and zonal west-to-east distance. The contour interval for vertical velocity is 0.4 m s^{-1}. Potential temperature is contoured every 2°C. Zonal velocity is contoured every 0.2 m s^{-1}.

b. Internal wave structure and evolution

The structure of the internal waves at peak amplitude is depicted in Fig. 5 showing plots of the vertical velocity, temperature, and horizontal velocity in the early morning at hour 38 as a function of depth and west-to-east distance. At this time, the internal waves have a wavelength of about 250 m and a displacement amplitude near 15 m. Beneath the thermocline, the internal waves are attenuated, indicating a reflection or absorption process. A plot of the wave vertical velocity at 50-m depth is shown in Fig. 6 as a function of time and horizontal distance including the time period of Fig. 5. The horizontal wave phase speed can be determined with this plot by calculating the slope of the maximum or minimum vertical motion as a function of time and distance (distance increases eastward). For the time period presented, the wave phase speed relative to a fixed location is steady at about -0.03 m s^{-1} and the wavelength is relatively constant throughout the cooling phase of the diurnal cycle. Relative to the undercurrent, which is moving at about 0.6 m s^{-1} at 50-m depth, the wave system is *always* propagating westward or upstream. The westward propagation is also shown in Fig. 5b where we note that upward-directed vertical velocity is located on the west side of the wave crests. The direction of wave propagation is important in determining the transport of momentum by the internal waves and is discussed in more detail later in this paper. Figure 6 also shows a disturbance propagating at approximately 0.08 m s^{-1} between hour 24 and 32. This disturbance can be identified in earlier cross-section plots (not shown) as a wave packet that moves westward or upstream with a horizontal group velocity, but at rate slower than the wave phase speed.

Although the model does not always produce a well-defined wave packet, the waves shown in Fig. 5 are similar in scale and strength to thermistor-chain measurements from Hebert et al. (1992) shown in Fig. 1. In particular, the wavelength, wave amplitude, and vertical coherence of the waves are consistent with the observations. Furthermore, the simulation shows indications of overturning in the surface layer as was observed. However, parameterized mixing limits the degree of wave steepening near the surface layer. Because of the periodic lateral boundaries, the simulations often have a quantized set of dominant wavelengths that match some integer multiple of the domain size. Nonetheless, the modeled wavelengths agree with the observed wavelength of the maximum amplitude spectral component reported in Moum et al. (1992). Also, the sustained strength of the model waves may be unrealistic because of the 2D system, which does not allow for horizontal wave dispersion in the meridional direction.

The simulated wave frequency for this case, which was about 0.5 cycles per hour (cph), does not agree with the dominant frequency measured by McPhaden and Peters (1992) during May and June 1987. They observed a diurnally varying disturbance with a much higher frequency (between 10 and 30 cph at depth 40 m). However, the current profile they reported (labeled 140W-1987 in Fig. 3) was significantly different from the initial conditions used here, with the surface current flowing eastward at approximately 0.6 m s^{-1} as compared to the -0.2 m s^{-1} current used here. Simulation

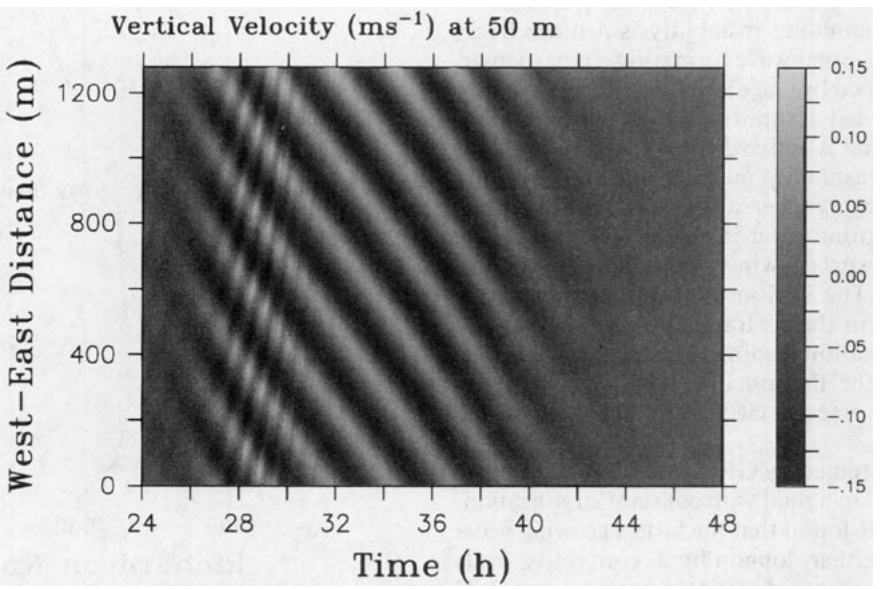

FIG. 6. Vertical velocity at 50 m as a function of time and zonal distance between hour 24 and 48 from case 134W-1987. This plot shows phase speed, wavelength, and frequency for the simulated internal waves.

results using the McPhaden and Peters data are presented later in this paper and show a Doppler-shifted wave system with wave frequencies agreeing with the observations.

c. *Wave generation and dissipation*

Two main conceptual models have been proposed to explain the formation of internal waves in the equatorial Pacific. In the first model, proposed by McPhaden and Peters (1992) and Moum et al. (1992), internal waves are directly forced by a Kelvin–Helmholtz instability that is active in the weakly stratified shear zone in the surface layer. The diurnal signal is forced by the nightly decrease in stratification and increased susceptibility to Kelvin–Helmholtz development. In the second model, or "obstacle effect" model, internal waves are forced by convective plumes that act as independent structures obstructing the mean flow much like topography (Wijesekera and Dillon 1991; Clark et al. 1986; Kuettner et al. 1987). Critical to the obstacle effect is a uniform horizontal flow in the mixed layer. For example, Hauf and Clark (1989) found that the velocity profile in their atmospheric simulations was always rapidly mixed to a uniform value in the boundary layer. As a result, convective plumes in the mixed layer were not sheared apart by the wind.

Our results indicate that, unlike the atmospheric boundary layer, the equatorial current shear is too strong for individual convective plumes to extend from the surface to the bottom of the mixed layer and block the flow, as required by the obstacle effect mechanism. In most cases with westward surface winds, the measured equatorial mixed layer velocity profile is not uniform because of the momentum flux from the wind stress. Because of the strong equatorial mixed layer shear, Kelvin–Helmholtz instability is a more likely mechanism for internal wave formation. In particular, the theory developed by Gage and Reid (1968, hereafter GR) gives a detailed account of a Kelvin–Helmholtz-type instability that is active during unstably stratified situations. This instability mechanism, known as the Tollmein–Schlichting (hereafter, T–S) mechanism, arises from the strong shear in the mixed layer that is generated by the surface wind stress opposing the undercurrent flow. The T–S instability generates an internal wave system that is trapped by the underlying shear and stratification leading to strong growth of internal waves in the thermocline. The wave trapping may also lead to a scale selection as discussed in the next section.

The problem studied by GR concerned the stability of a Poisseuille jet in a fluid with constant stratification. In their study, GR found that the fastest growing wave modes formed either longitudinal convective rolls aligned along the shear direction, or transverse T–S waves, depending on the value of the Rayleigh number and Reynolds number of the flow. For unstable flows with a high Reynolds number (i.e., strong shear), transverse T–S waves were shown to be the most unstable mode, while a high Rayleigh number (i.e., strong cooling) led to a longitudinal convective roll instability. The T–S mechanism was active if the Richardson number was less than 0.05. In all cases, the critical Reynolds number for onset of the transverse wave instability was found to be 5400.

The conditions studied by GR, namely, constant stratification and Poisseuille flow, do not directly apply to the equatorial oceanic flow problem. However, an estimate of the Reynolds number for turbulent flow in the equatorial system can be calculated using

$$\mathrm{Re} = \frac{U_x d}{2K_m}, \tag{17}$$

where U_x is a velocity scale for the mixed layer, d is the mixed layer depth, and K_m is the eddy viscosity. Estimates of these parameters for the equatorial problem are that $U_x = 0.5$ m s^{-1}, $d = 30$ m, and $K_m = 0.001$ m^2 s^{-1} yield a Reynolds number of about 7500, which is of the correct order to indicate that the T–S instability is possible in the surface mixed layer [estimate of K_m from Peters et al. (1988); U_x and d from Moum et al. (1992)]. In addition to the requirement on Reynolds number, GR also noted that a Richardson number of

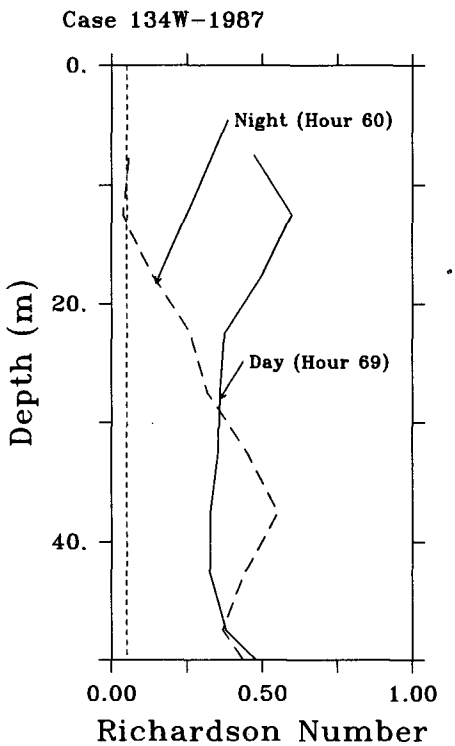

FIG. 7. Gradient Richardson number calculated at hour 60 (night) and hour 69 (day) for case 134W-1987. The small dashed line represents a constant Richardson number of 0.05.

less than 0.05 was required in cases where the fluid was uniformly stratified. As shown in Fig. 7, the simulated surface-layer Richardson number defined as

$$\mathrm{Ri} = -\frac{g}{\rho}\frac{\partial \rho}{\partial z}\Big/\left(\frac{\partial u}{\partial z}\right)^2 \tag{18}$$

alternates between values below 0.05 during the night to values above 0.05 during the daytime, agreeing with this condition.

To more clearly demonstrate the simulated Kelvin–Helmholtz instability process, a high-resolution simulation (grid size 512 × 120, grid spacing 2.5 m) was performed using the 134W-1987 initial conditions. A time series plot of potential temperature for this experiment is presented in Fig. 8 at hour 4, 4.5, and 5 showing a subregion of the model domain that concentrates on two wave crests in the internal wave system. The wave system in Fig. 8 rapidly amplifies and eventually forms regions of overturning circulations or resolved two-dimensional turbulence. The overturning regions are quickly restratified in the model by the action of increased subgrid-scale mixing, which acts to smooth disturbances in a manner consistent with actual 3D turbulence.

The Kelvin–Helmholtz instability shown in Fig. 8 is forced by a pressure disturbance that results from the background shear flow being deflected by the wave surface. The pressure force overcomes the buoyancy associated with stratification, leading to wave amplification (see Turner 1973, pp. 93–94). Waves are strengthened when the net vertical acceleration with each wave crest (trough) is upward (downward) causing an increase in the wave amplitude. Comparison of the combined pressure and advection

$$-\frac{\partial P}{\partial z} - u\frac{\partial w}{\partial x} \tag{19}$$

term to the buoyancy

$$-g\frac{\rho'}{\rho_0} \tag{20}$$

term from the vertical momentum equation (2) (Fig. 9) at a wave crest (vertical line in Fig. 8) shows that the pressure term exceeds the buoyancy term as implied by theory (the advection term is added to the pressure term to remove the vertical acceleration caused by the wave propagation). The difference between these two terms explains the net upward vertical acceleration shown by the solid line in Fig. 9. Similar values for these terms are found at the wave troughs; however, the sign of the individual terms is reversed.

Also supporting a Kelvin–Helmholtz-type disturbance is the horizontal phase speed of the waves. In all of the cases examined in this paper, the wave phase speed matches the horizontal velocity somewhere within the low Richardson number mixed layer where the waves are forced. This matching is consistent with both theory and observations of Kelvin–Helmholtz instability formation (Turner 1973).

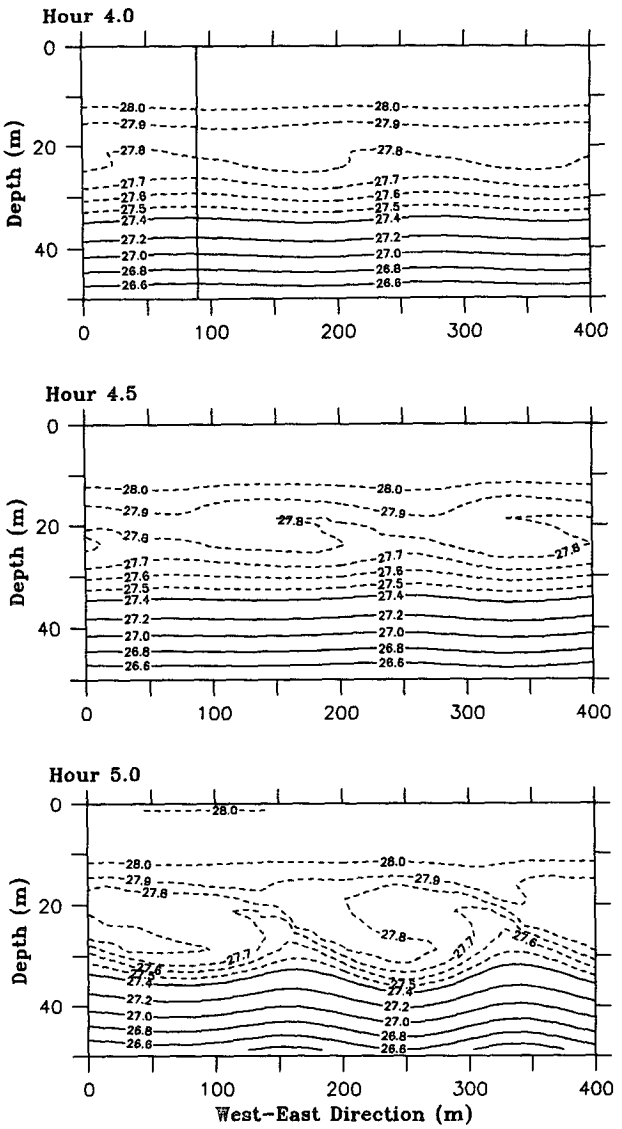

FIG. 8. Potential temperature between hour 4 and 5 from case 134W-1987 over a subregion of the high-resolution grid (see text). Contour interval is 0.2°C for solid lines and 0.1°C for dashed lines. The vertical line in the hour 4 plot represents the location of the vertical momentum analysis shown in Fig. 9.

d. Horizontal scale selection

A key aspect of the internal wave maintenance concerns the trapping of the internal waves by the underlying ambient shear and density structure. The velocity and density structure may also determine the horizontal scale of the internal waves. To examine these effects, we used CTD data reported in Moum et al. (1989) from the 1984 Tropic Heat I Experiment as a model initialization (designated case 140W-1984). We se-

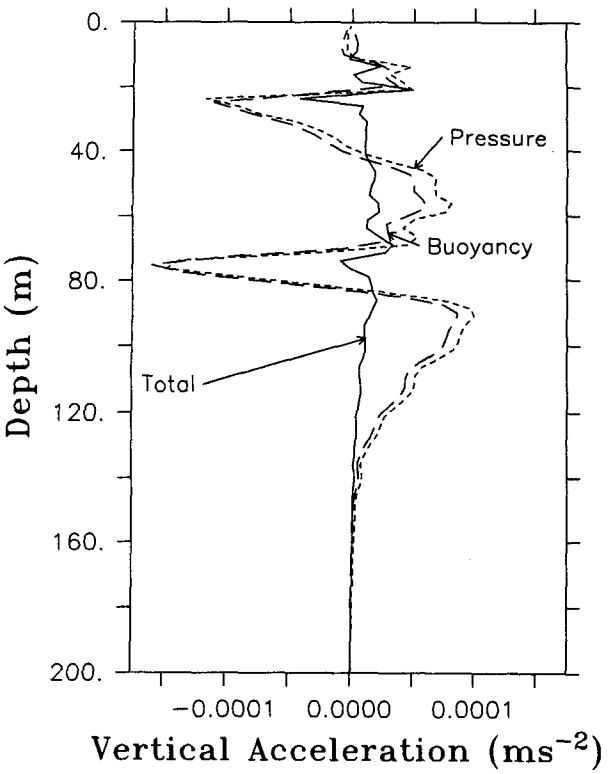

FIG. 9. Directly calculated terms from the vertical momentum equation (2) for pressure and buoyancy acceleration with the horizontal advection term added to eliminate vertical accelerations due to the wave propagation at hour 4 (nighttime) from the high resolution 134W-1987 case. These terms are calculated for a vertical column at west–east location of 90 m shown as a vertical line in Fig. 8 at hour 4.0.

lected this case because the vertical temperature and velocity structure measured in 140W-1984 strongly differed from 134W-1987, although both cases featured a diurnal cycle in turbulent dissipation rates. Also, strong evidence of internal wave activity was observed during the 140W-1984 experiment period (Wijesekera and Dillon 1991; Brainard and McPhaden 1992). The goal of this simulation was to examine what factors, such as the strength of stratification or current shear, determine internal wave scales of motion.

The data used as initial conditions were measured 28 November 1984 at 140°W on the equator. The temperature profile for this experiment (Fig. 2, labeled 140W-1984) was normal for the observing period with a surface mixed layer to about the 30-m depth and a strong thermocline throughout the undercurrent core. However, the large maximum velocity of the EUC during the observing period was not representative of fall conditions, when the undercurrent core velocity is usually at a yearly minimum between 0.5 and 1.0 m s^{-1} (McPhaden and Taft 1988). The combination of a stronger than normal undercurrent with a consistent wind stress of −0.1 N m^{-2} leads to a deep shear layer (~70 m) between the core and the surface, with a Richardson number between 0.25 and 0.35. Within this region, the turbulent dissipation rate had a strong diurnal cycle, varying between approximately 10^{-6} W kg^{-1} during the night to less than 10^{-7} W kg^{-1} during the day.

Initially, we performed a 3-day simulation with these data using a wind stress of −0.1 N m^{-2} and the same model dimensions as the 134W-1987 case. However, the preliminary model run showed that the characteristic wavelength for the 140W-1984 case was too long for the former domain size. Therefore, we increased the horizontal and vertical domain sizes to 2560 m and 400 m, respectively. As in the 134W-1987 case, we found that the internal waves have a diurnal signal with peak wave intensity near sunrise and that the wave phase velocity, −0.3 m s^{-1} (Fig. 10), matches the velocity range in the mixed layer. Our results also show good agreement between the diurnal cycle of the simulated isopycnal displacement and climatological observations calculated by Brainard and McPhaden (1992). For the month of November 1984 they found a statistically significant diurnal cycle in internal wave activity above 100 m as indicated by the isopycnal displacement variance. Below the undercurrent, a statistically significant diurnal cycle was not identified. However, the overall displacement variance below 100 m was 2–3 times larger than the surface variance, which could have overwhelmed a weak diurnal signal. As shown by comparing Fig. 10 to Fig. 6, case 140W-1984 produced more discrete wave packets and wave phase speed changes as a function of time (e.g., between hour 26 and 28), when compared with the 134W-1987 case. The wave packets have a group velocity of about 0.35 m s^{-1}, which is again westward relative to the background flow indicating westward energy transport. The largest difference between the 1984 and 1987 experiments is the horizontal scale of the simulated internal waves (Fig. 11). In the 1984 case, the wavelength of the internal waves was about 500 m, compared with only 250 m for the 1987 case.

A possible explanation for the differing wavelength can be found by analyzing the linear wave characteristics of the modeled flow. As noted earlier, the vertical structure of stratification and shear can trap the internal wave system leading to wave amplification and a maximum disturbance wavelength. The critical wavenumber that divides evanescent or trapped linear internal wave modes from vertically propagating modes is

$$\lambda_{\max} = \frac{2\pi}{l}, \tag{21}$$

where

$$l = \left(\frac{N^2}{(U-C)^2} - \frac{\partial^2 U/\partial z^2}{(U-C)} \right)^{1/2}. \tag{22}$$

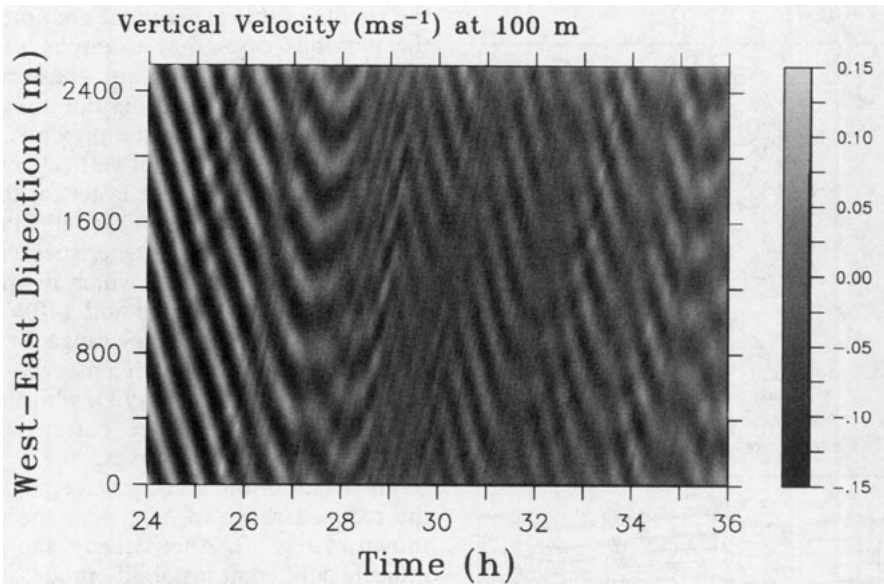

FIG. 10. Vertical velocity at 100 m as a function of zonal distance between hour 24 and 36 from case 140W-1984.

Here U is the mean zonal velocity, and C is the wave phase speed (Smith 1979). Waves with a horizontal wavelength, λ, greater than λ_{max} are vertically propagating and have both a horizontal and vertical wavenumber and group velocity. When $\lambda < \lambda_{max}$, internal waves are evanescent and do not have a vertical wave structure or group velocity but decay exponentially with depth. A plot of the λ_{max} using the temperature and velocity fields for 140W-1984 and 134W-1987 is shown in Fig. 12. For the 134W-1987 case, this figure shows that waves with wavelengths greater than 250–300 m vertically propagate energy downward, while shorter wavelength waves are trapped. Likewise, λ_{max} for the 140W-1984 case is between 400 and 500 m, which compares favorably with the simulated wave system shown in Fig. 11.

The vertical density and shear structure modulates the internal waves forced by the T–S instability. Disturbances with wavelengths greater than λ_{max} shown in Fig. 12 cannot grow because they lose energy through vertical propagation. This leads to a dominant disturbance wavelength near λ_{max} assuming that the instability amplification is maximum for a disturbance wavelength greater than λ_{max}. If the wavelength of maximum instability is less than λ_{max} for a significant depth, then the wave system will show a vertical phase shift indicating wave propagation. Rosenthal and Lindzen (1983) discuss a similar process for overreflecting internal gravity waves where waves amplify by reflecting between an unstable critical level and a solid boundary. In the analogous equatorial situation, the solid boundary is replaced by the evanescent layer with the T–S instability acting as the internal wave energy source.

An alternate explanation for the wave scales is provided by Kelvin–Helmholtz instability theory for stratified flows as discussed in Moum et al. (1992). They applied a horizontal scaling equal to $2\pi h$, where h is the depth of the low Richardson number layer (<0.5) for each case (Turner 1973, p. 99). Using the observed profiles, h is approximately 40 m for 134W-1987 and 70 m for 140W-1987, giving horizontal wavelengths of 250 and 440 m, respectively, which are similar to the model results. It is likely that the Kelvin–Helmholtz instability simulated by the model is scaled by a combination of the linear trapping wavelength and the inherent scale for the instability.

e. Wave momentum transport

Eliassen and Palm (1960) note that for linear waves the transfer of momentum between an internal gravity wave and the ambient flow can only occur in the vicinity of a critical level. In the simulations shown thus far, a critical level did not exist below the mixed layer because the horizontal velocity below the undercurrent core did not equal the mixed layer velocity or internal wave phase speed. However, profiles are frequently observed in late spring and early summer that have surface velocities matching the current velocity just below the undercurrent core (McPhaden and Taft 1988). To examine a case with a critical level, we used the averaged zonal velocity and temperature profile given in McPhaden and Peters (1992) that was measured between 12 May and 11 June 1987 at 140°W on the equator (Fig. 2, labeled 140W-1987). This profile differs from the previous model initial conditions by having an eastward surface current velocity equal to the zonal

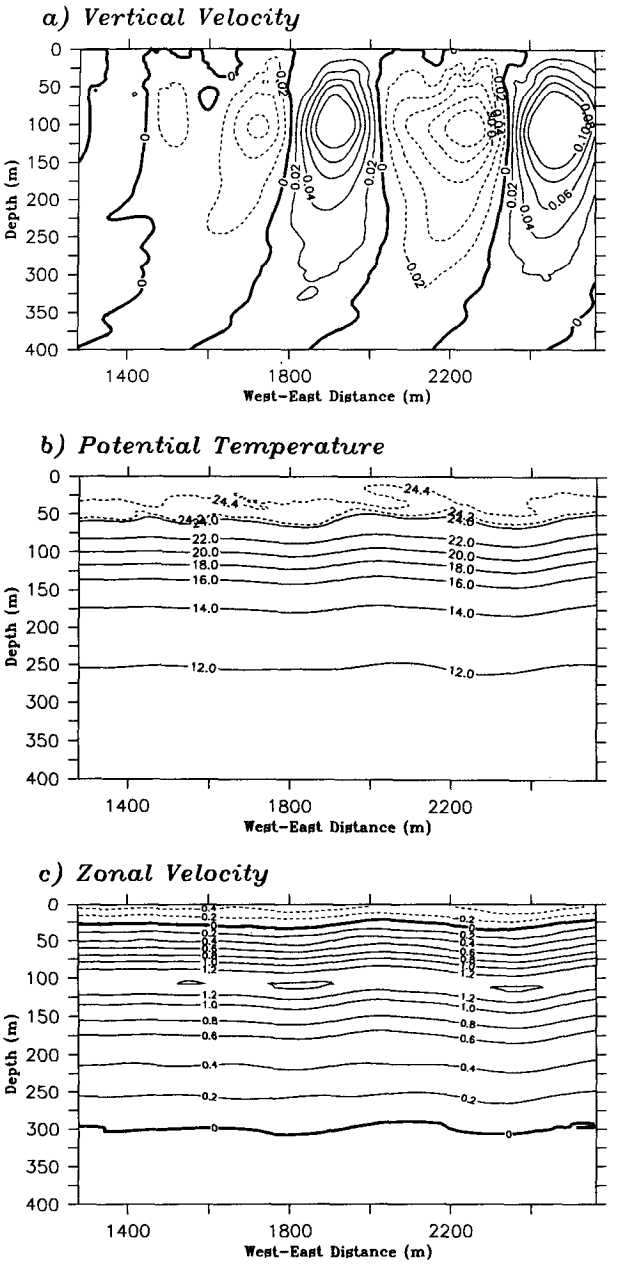

FIG. 11. Vertical velocity (a), potential temperature (b), and zonal velocity (c) for hour 38 (early morning) from the 140W-1984 case as a function of depth and zonal west-to-east distance. The contour interval for vertical velocity is 0.02 m s^{-1}. Potential temperature is contoured every 2°C, with contours greater than 24.0°C plotted as dashed lines every 0.2°C. Zonal velocity is contoured every 0.2 m s^{-1}. This plot represents only half of the simulated horizontal domain for case 140W-1984.

velocity just below the undercurrent core at about 150 m.

A plot of the simulated temperature, vertical velocity, and horizontal velocity for this case at hour 32 is presented in Fig. 13. Other than the diurnal wave cycle, the results of this experiment are quite different from the previous cases. For example, the vertical wave structure shows a significant phase shift with depth, indicating that the waves are not immediately evanescent, as was the case in the previous simulations. As shown by the phase plot of vertical velocity in Fig. 14, the wave phase speeds are faster for this case at about 0.6 m s^{-1} with shorter wavelengths between 150 and 200 m. These wave characteristics yield a wave frequency of about 12 cph, which is much higher than the 134W-1987 (0.5 cph) and 140W-1984 (2.5 cph) cases. The higher frequency range for the 140W-1987 case is in agreement with observations reported by McPhaden and Peters (1992), who suggested that the stronger eastward surface current caused Doppler shifting of the internal waves.

The cause of the vertical wave phase shift might be the reduced range of λ_{max} near the critical level, as shown in Fig. 12. Alternatively, the phase shift may indicate a different instability mode, such as described in Hazel (1972). Hazel performed a linear stability analysis for Kelvin–Helmholtz-type instabilities using the Taylor–Goldstein equation and examined various velocity and stability profiles, but only for positive Richardson numbers. For a case with a sech(z) velocity profile (Bickley jet) and constant stratification, Hazel found that two instability modes existed. The first mode, called the sinuous mode, had a vertical structure resembling the results from the 134W-1987 and 140W-1984 cases. For the second mode, called the varicose mode, a 90° phase shift was predicted, giving a vertical structure similar to the present case. Comparison of the numerical results presented here to Hazel's work is only qualitative because the profiles and forcing are not equivalent for both cases.

The interaction of internal waves with a critical level is discussed in detail by Booker and Bretherton (1967) for stratified fluids having a Richardson number greater

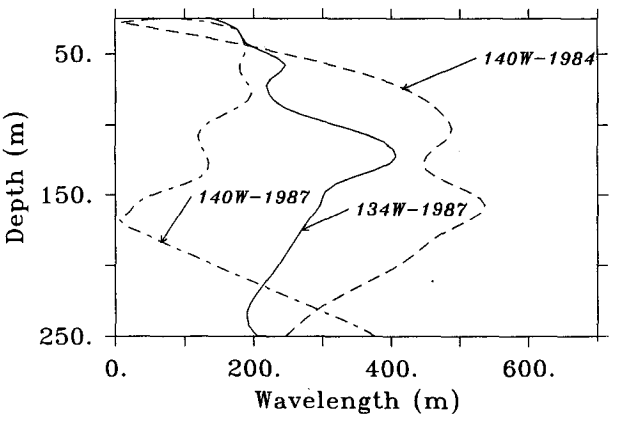

FIG. 12. Characteristic internal wave horizontal scales as determined by linear theory (see text) for each initialization profile. This figure shows that the internal wave wavelengths predicted by the numerical model for each case are consistent with simplified theory.

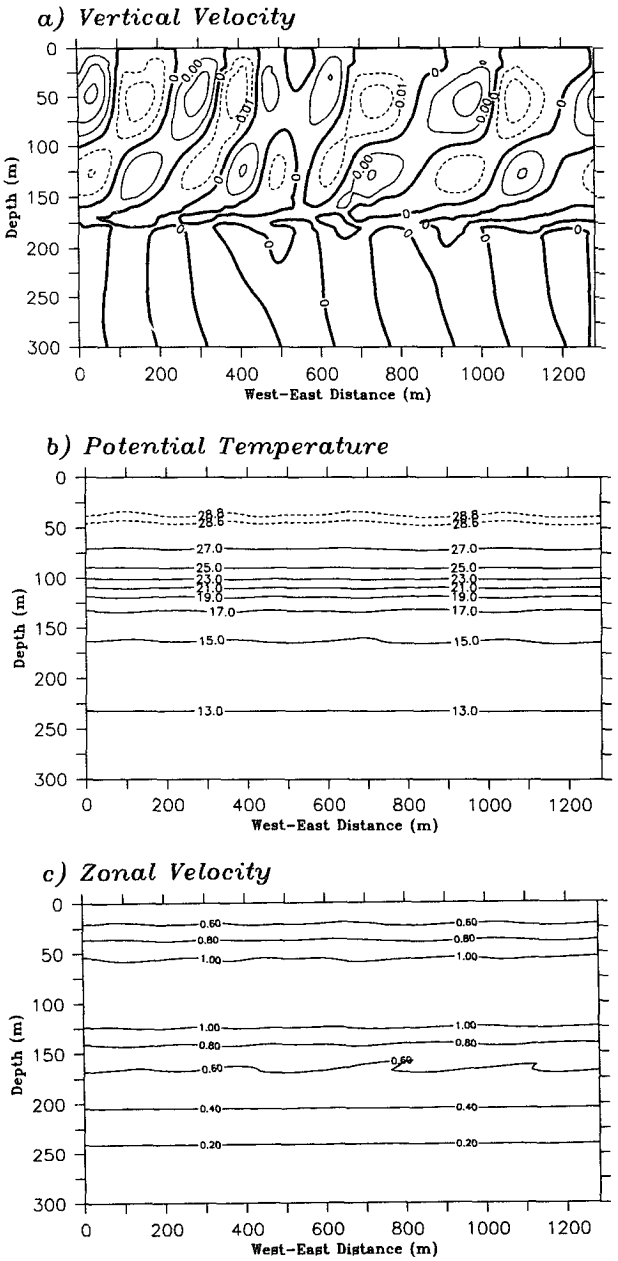

FIG. 13. Vertical velocity (a), potential temperature (b), and zonal velocity (c) for hour 32 from the 140W-1987 case as a function of depth and zonal west-to-east distance. The contour interval for vertical velocity is 0.01 m s^{-1}. Potential temperature is contoured every 2°C, with contours greater than 28.6°C plotted as dashed lines every 0.2°C. Zonal velocity is contoured every 0.2 m s^{-1}.

than 1/4, and by Lindzen and Barker (1985) for situations with the Richardson number below 1/4. When the Richardson number is greater than 1/4, the critical level acts as an absorbing layer with internal waves *losing* energy and momentum to the background flow (Booker and Bretherton 1967; also see Turner 1973, Fig. 2.15; or Winters and D'Asaro 1989). As the internal waves approach the critical level, their vertical wavelength decreases, eventually leading to wave overturning and increased mixing. The momentum transported by the internal waves is transferred to the background flow during the absorption process. The decrease in vertical wavelength in the present case is noticeable in Fig. 13 above 175 m where the vertical velocity tends to fold over with depth. Because the Richardson number is greater than 1/4 at the critical level for this case, the waves are not reflected and lose momentum to the mean flow. As a consequence, the waves are weaker in amplitude (by about a factor of 5) than the evanescent waves in the 134W-1987 case (see Fig. 5).

Estimates of the modeled average momentum change can be made by calculating the difference in the horizontally averaged zonal current at two model output times. A plot of the rate of change of the zonal velocity between day 1 and 3 for each of the experiments, 134W-1987, 140W-1984, and 140W-1987, is present in Fig. 15. The three cases show a significant difference in the momentum flux with the 134W-1987 and 140W-1984 cases having a minimum above the undercurrent core, while the 140W-1987 case has a minimum below the undercurrent core at 150 m, near the critical level location. The absolute momentum transfer for all cases is nearly equivalent with a minimum value near -5×10^{-7} m s^{-2}, which compares to calculations by Hebert et al. (1991) of the pressure gradient and nonlinear advection terms ($\approx -3 \times 10^{-7}$ m s^{-2}) for the observed equatorial momentum budget. This correspondence is encouraging, given that the model does not have explicit terms, such as the large-scale equatorial pressure gradient, describing the balance of horizontal forces. The results presented here indicate that internal waves are an important term in the momentum balance.

The simulated horizontally averaged zonal momentum change shown in Fig. 15 can be divided into three terms from the horizontal momentum equation (1): 1) the directly calculated horizontally averaged wave stress divergence, $\partial(uw)/\partial z$, which can be approximated as $w\partial u/\partial z$; 2) the subgrid-scale parameterization of turbulent mixing,

$$\frac{\partial}{\partial x}(u''^2) - \frac{\partial}{\partial z}\overline{(u''w'')};$$

and 3) the ∇^{12} numerical filter (Fig. 16). Plots of these terms for each case, 134W-1987, 140W-1984, and 140W-1987, are shown in Figs. 16–18, respectively. The numerical filter is plotted to show that it has a small influence in comparison to the other transport terms. Other terms in (1), such as the pressure gradient and horizontal advection by u, average to near zero over the domain and are not shown. In all of the experiments, the positive wave stress divergence in the mixed layer near the surface shows that westward mo-

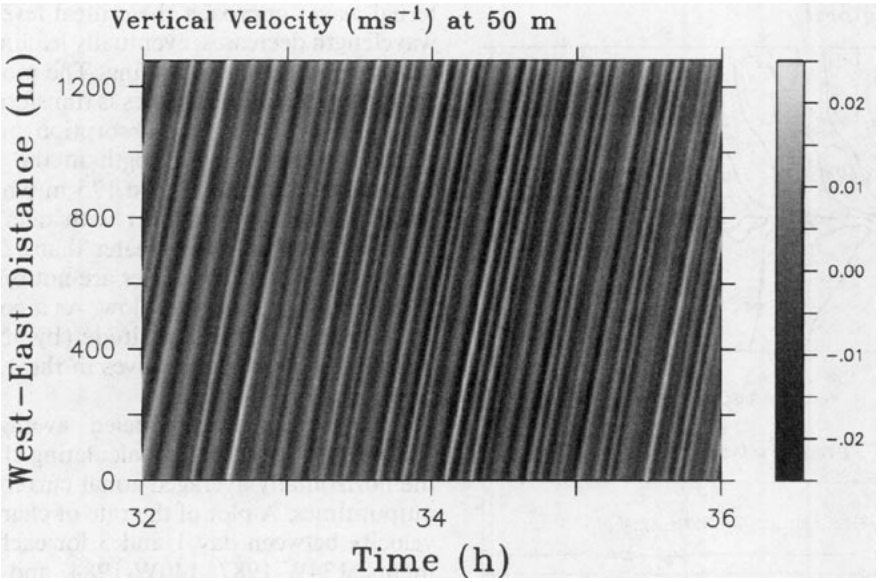

FIG. 14. Vertical velocity at 50 m as a function of zonal distance between hour 32 and 36 from case 140W-1987.

mentum is transferred from the mean flow to the internal waves. Normally, this momentum transfer would result in an increase in the local eastward flow velocity, but in these cases, the subgrid-scale mixing of westward momentum from the surface wind stress reduces the effect of the momentum transfer to the wave system. As a result, the net velocity actually decreases in this part of the vertical profile for case 140W-1987 and 134W-1987 during the 2-day period.

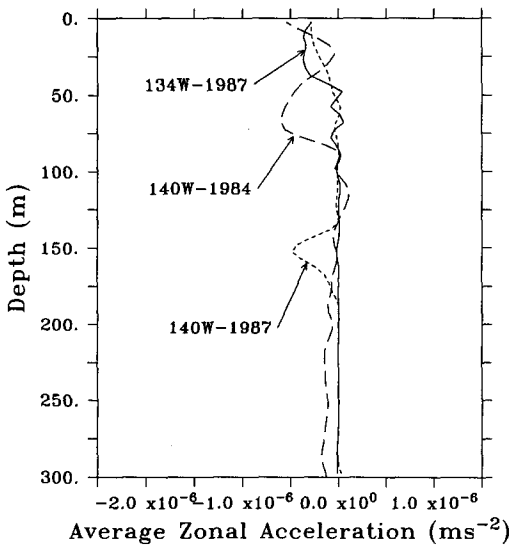

FIG. 15. The average rate of zonal velocity change during day 2 and 3 for case 134W-1987, 140W-1984, and 140W-1987. This plot is calculated by differencing the horizontally averaged zonal velocity component at hour 24 and hour 72 and dividing by 2 days.

The transfer of westerly momentum back to the mean flow, as indicated by a negative wave stress divergence, differs in location with each case. For example, most of the westerly momentum transfer in cases 134W-1987 and 140W-1984 is above the undercurrent core, as compared to case 140W-1987 where the strongest negative stress divergence is below the undercurrent core. The difference in behavior between these cases results from the vertical wave propagation and critical level absorption that are evident in the 140W-1987 case. The wave stress divergence at the critical level in the 140W-1987 case accounts for almost all of the westward momentum transport back into the mean velocity profile. In the 140W-1984 case, a small but significant wave stress divergence is also noted below the undercurrent core. This small flux is most likely a result of the wave system approaching a critical level near the bottom of the model domain. The internal waves for this case have more vertical extent because of the deeper location of the maximum wave vertical velocity (roughly 100 m for this case versus 50 m for 140W-1987). As a result, internal wave motions are still significant at depths where the mean flow is near the wave phase speed, especially for the slower moving components as shown in Fig. 10 around hour 28.

The transfer of westward momentum from the internal waves to the mean flow at the critical level contrasts with the conceptual model of Wijesekera and Dillon (1991), who assumed that critical levels would not exist below the undercurrent. They argued that internal waves generated at the base of the mixed layer must propagate westward, relative to a fixed location, to transport westward momentum. The 140W-1987 case clearly demonstrates that westward propagating

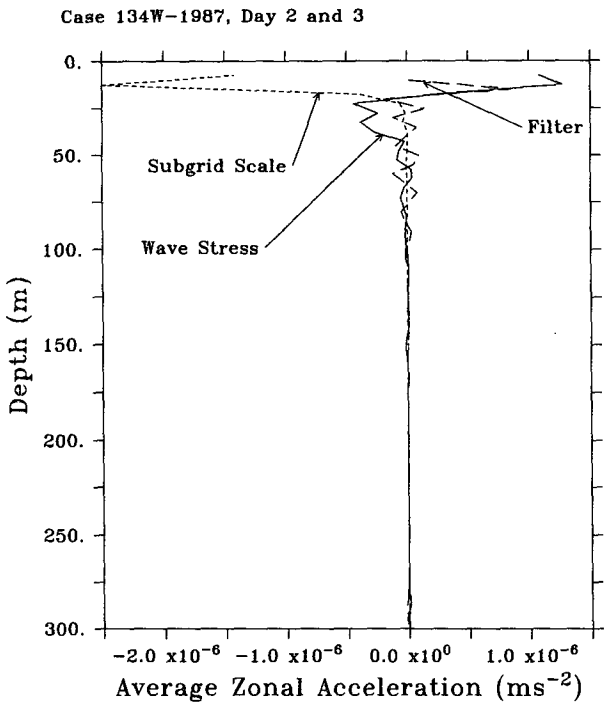

FIG. 16. Directly calculated terms from the zonal momentum equation (1) describing the vertical advection, the subgrid-scale mixing, and the numerical filtering of the zonal velocity component. These terms are averaged over the horizontal domain and over day 2 and 3 of the 134W-1987 simulation, corresponding to the period considered in Fig. 15.

waves are not needed for westward momentum transport. Both the diurnal internal wave cycle and the internal wave transport of westward momentum were still simulated in the 140W-1987 case, even though the surface current velocity was eastward at 0.6 m s^{-1}.

The absolute direction of wave propagation is not the critical parameter for determining the direction of wave momentum transport. The important variable is the direction of wave propagation relative to the undercurrent and the existence of a velocity at depth that equals the wave phase velocity. For example, in the 140W-1987 case the waves move eastward at 0.6 m s^{-1} relative to a fixed point. This velocity matches the mean flow within the mixed layer where the waves form, but is less than the 1.2 m s^{-1} flow velocity in the undercurrent core. Below the undercurrent core, the mean flow again equals the wave phase speed at a critical layer near 150 m, where the waves transfer their westward momentum by decelerating the mean flow. Between the wave formation depth in the mixed layer and the critical level, the waves propagate westward or upstream relative to the mean current, implying a westward momentum transport. The movement of the waves is much like a fish swimming upstream (westward) at a speed slower than the (eastward) stream flow rate. To the observer onshore, the fish is moving downstream or eastward, but at rate less than the stream flow. However, as far as the fish is concerned, it is moving westward and carrying westward momentum. More formally, the waves in case 140W-1987, which carry westward momentum, travel eastward simply because the observation reference frame is moving toward the east at a velocity greater than the wave phase speed.

Interaction of internal waves at a critical layer can generate regions of strong mixing as momentum is transferred from the internal waves to the background flow (Winters and Riley 1992). Jones (1973) describes a well-mixed water mass, referred to as 13°C Water, located below the undercurrent core that may result in part from critical layer mixing. High-frequency measurements below the undercurrent core are needed to see if internal waves are indeed transporting momentum to these depths when the surface currents are eastward and favor critical layer development.

f. Wind stress variation effects

A final three-day experiment was performed to examine the importance of the wind stress direction on modeled internal waves by applying a time-dependent wind stress that changed from westerly to easterly near the middle of the model run. For the initial 12 h of the simulation, the wind stress was set to the 134W-1987 case value of −0.025 N m^{-2} to allow spinup of the internal wave system. Between 12 and 24 h, the

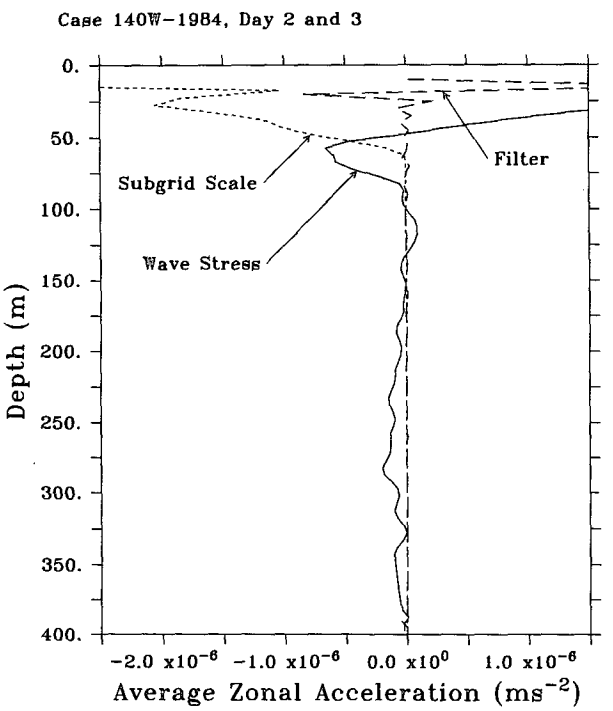

FIG. 17. Same as Fig. 16 but for case 140W-1984.

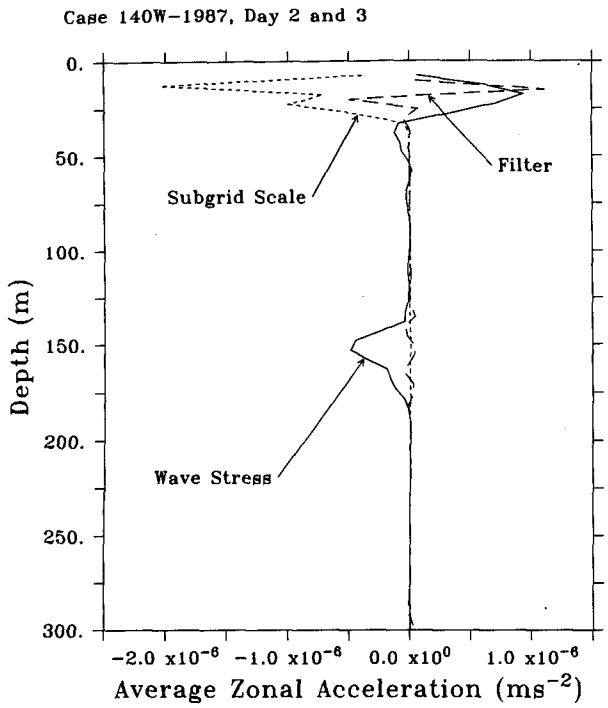

FIG. 18. Same as Fig. 16 but for case 140W-1987.

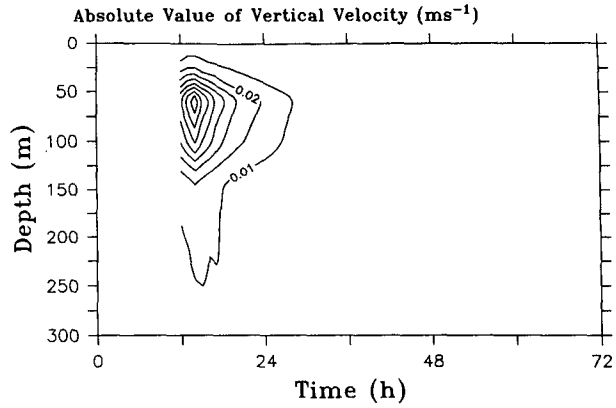

FIG. 19. Simulated horizontally averaged absolute value of vertical velocity as a function of time for the 134W-1987 case with increasing surface wind stress from -0.025 N m^{-2} to 0.01 N m^{-2}. Contour interval is 0.01 m s^{-1}. When compared to Fig. 3b, this plot shows the effect of wind stress reversal on the internal wave diurnal cycle.

wind stress was linearly increased to a value of 0.01 N m^{-2} to simulate the onset of a westerly wind burst. A plot of the resulting wave intensity, as measured by the absolute value of the vertical velocity, is shown in Fig. 19. Comparison of this figure to Fig. 4 illustrates that the direction of the surface wind stress is critical to both the wave formation and maintenance. Specifically, the reversal in wind stress eliminates the strong diurnal cycle in wave intensity and causes an overall weakening of the internal wave activity. The crucial parameter in this simulation is the value of the shear strength in the mixed layer (Fig. 20). When the surface winds are eastward, the mixed layer shear decreases with a commensurate decrease in Re. As noted earlier, the T–S instability requires a Reynolds number greater than some critical value (5400 for the simplified theoretical case). Here, the decrease in the mixed layer shear leads to a reduction in the T–S instability and internal waves are not generated. Therefore, in this case the momentum budget of the surface layer is balanced by a local change in the current velocity, rather than by an increase in vertical transport of momentum by internal waves.

4. Summary and conclusions

Using a 2D nonhydrostatic numerical model, we have successfully simulated the generation and evolution of internal waves in the equatorial Pacific. The internal wave growth characteristics are consistent with a Kelvin–Helmholtz instability known as the Tollmein–Schlichting (T–S) instability mechanism as discussed in Gage and Reid (1968). In an idealized case, the instability requires both a Richardson number less than 0.05 and a Reynolds number greater than 5400. In our simulations, we found that the wave intensity is dependent on these parameters, although an exact comparison could not be made between the theoretical parameter values and the model results. Nonetheless,

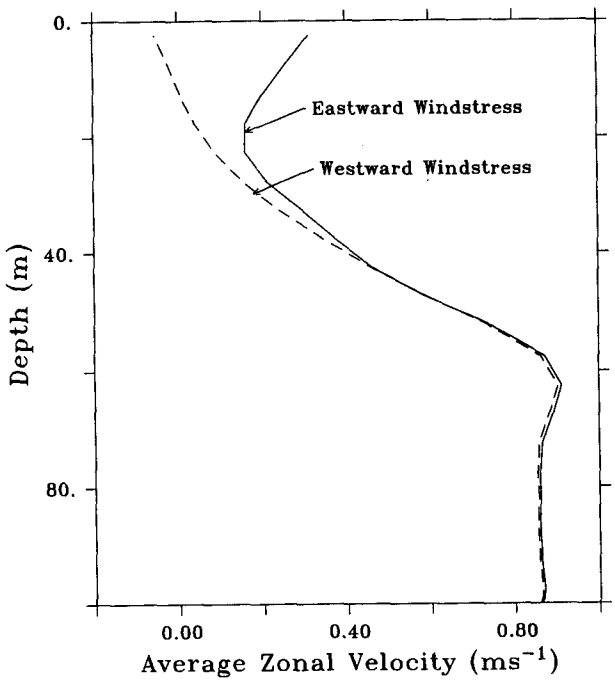

FIG. 20. Vertically averaged horizontal velocity for case 134W-1987 with eastward and westward wind stress at hour 38. The average shear above 40 m is lower for the eastward wind stress case.

both the wave diurnal cycle and the sensitivity of the internal waves to wind direction could be linked to the shear and density stratification requirements of the T–S instability.

In general, we found that the horizontal scale of the internal waves was dependent on a critical wavelength that is approximately equal to the ratio of the Brunt–Väisälä frequency to the background flow velocity. Waves that were less than this critical wavelength were effectively trapped within the thermocline and amplified by reflecting energy gained from the T–S instability. For the 134W-1987 case, both the wavelength (~250 m) and wave amplitude (~15 m) of the simulated mode agreed with observations of vertically coherent internal waves reported in Moum et al. (1992) and Hebert et al. (1992). Likewise, the wave frequency for the 140W-1987 case, which varied between 10 and 12 cph, was in agreement with measurements of diurnally varying disturbances taken by McPhaden and Peters (1992). The high-frequency of the simulated waves was a result of Doppler shifting by a strong eastward surface current, supporting the Doppler shift hypothesis given by McPhaden and Peters (1992).

Previous models of momentum transport in the equatorial Pacific required a westward moving surface current and related convective eddy field for wave formation and westward momentum transport. Our results show that the important parameter for wave momentum transport is the direction of wave propagation *relative to the background current.* The simulated wave phase speed was westward or upstream in all cases, indicating a transport of westward momentum, even though the waves were in one case (140W-1987) moving eastward relative to a fixed location. This result clarifies the problem discussed in McPhaden and Peters (1992) concerning the need for a westward surface current. They noted that, based on the observed climatology, the requirement for a westward surface current could not be fulfilled for 3 to 4 months each boreal spring. The simulations presented here indicate that westward momentum transport can occur above the undercurrent core, without requiring a westward surface current. The results also show that critical levels can exist beneath the undercurrent core and lead to significant momentum transfer from the surface to the critical level depth. High temporal and spatial resolution measurements of temperature, salinity, and velocity are needed above and below the undercurrent core to verify these conclusions.

Observations by Moum et al. (1992) suggest that equatorial internal wave activity is directly related to sustained westward wind stress. When the observed wind stress direction was eastward (i.e., relaxation of the trade winds), internal waves were not detected in the observations. We noticed a similar response with the model when the wind stress direction was reversed from westward to eastward. Within a day of the simulated wind reversal, the formation of internal waves ceased, agreeing with the observed behavior. For this case, the linkage between wind stress and wave formation was the strength of the shear in the mixed layer. When the wind stress direction was eastward, the average vertical shear in the horizontal current decreased at the surface. This in turn led to a decrease in the mixed layer Reynolds number and a reduction in the T–S instability.

The model results indicate that improved parameterizations may be needed to account for internal wave momentum transport in large-scale models of the equatorial region. This is particularly true for periods when a critical level exists below the undercurrent core. For these cases, construction of a parameterization for the internal wave momentum flux would involve both internal wave phase speed estimates and a turbulence closure at the wave critical levels. Unlike most turbulence parameterizations that deal with only local conditions, an internal wave stress parameterization would need to identify the prominent internal wave modes and then force mixing at the mode critical levels. These would vary in depth according to the surface-layer conditions and the underlying shear structure. In a future study, we plan to investigate the scale of maximum instability for Kelvin–Helmholtz waves by numerically solving the Taylor–Goldstein equation with the profiles used here. This will provide a more quantitative analysis for comparison to the model results and future observations and may lead to a simplified model for the basis of a parameterization.

In summary, our simulation results indicate that the growth of internal waves in the equatorial oceans is a result of a Kelvin–Helmholtz type instability that is strongly tied to the surface-layer shear strength and Richardson number. When the Richardson number is below 0.05, waves tend to grow, while higher Richardson numbers lead to wave decay. Wave growth is forced by a Kelvin–Helmholtz instability that is dependent on both a low static stability and a strong vertical current shear. During conditions of moderate to strong westerly wind stress, a diurnal cycle of internal wave activity is simulated by the model as the surface-layer Richardson number oscillates in response to the changing static stability. If the wind stress is weak or reversed, then mixing forced by nighttime cooling destroys the surface-layer shear zone, preventing internal wave growth and the diurnal cycle. Finally, the simulations support the hypothesis that internal waves can be important components in the momentum budget of the equatorial oceans and should be considered in models of the large-scale equatorial circulation.

Acknowledgments. We would like to thank Russell Brainard and Drs. John Downing, Theresa Paluszkiewicz, Dave Hebert, Jim Moum, and Richard Romea for their helpful suggestions, data, and comments. We would also like to thank the TOGA-TAO Project Office of NOAA/PMEL, Dr. Michael J. McPhaden, Director;

Mike Riches (U.S. DOE Environmental Sciences Division) for his support and encouragement; and the extremely helpful suggestions by the anonymous reviewers. This study was funded by the U.S. Department of Energy as part of the CO_2 Oceans Program at the Battelle/Marine Science Laboratory. The Battelle/Marine Science Laboratory is part of the Pacific Northwest Laboratory, which is operated for the U.S. Department of Energy by Battelle Memorial Institute under Contract DE-AC06-76RLO 1830.

REFERENCES

Allen, D. J., A. R. Douglass, R. B. Rood, and P. D. Guthrie, 1991: Application of a monotonic upstream-biased transport scheme to three-dimensional constituent transport calculations. *Mon. Wea. Rev.*, **119,** 2456–2464.

Booker, J. R., and F. P. Bretherton, 1967: The critical layer for internal gravity waves in a shear flow. *J. Fluid Mech.*, **27,** 513–539.

Brainard, R. E., and M. J. McPhaden, 1992: Diurnal variability of high-frequency internal waves in the upper equatorial Pacific Ocean. *Abstract, AGU Fall Meeting, Eos,* **73,** 320–321.

Bryden, H. L., and E. C. Brady, 1985: Diagnostic model of the three-dimensional circulation in the upper equatorial Pacific Ocean. *J. Phys. Oceanogr.*, **15,** 1255–1273.

Clark, T. L., T. Hauf, and J. P. Kuettner, 1986: Convectively forced internal gravity waves: Results from two-dimensional numerical experiments. *Quart. J. Roy. Meteor. Soc.*, **112,** 899–925.

Colella, P., 1990: Multidimensional upwind methods for hyperbolic conservation laws. *J. Comput. Phys.*, **87,** 171–200.

Deardorff, J. W., 1980: Stratocumulus-capped mixed layers derived from a three-dimensional model. *Bound.-Layer Meteor.*, **18,** 495–527.

Dillon, T. M., J. N. Moum, T. K. Chereskin, and D. R. Caldwell, 1989: Zonal momentum balance at the equator. *J. Phys. Oceanogr.*, **19,** 561–570.

Eliassen, A., and E. Palm, 1960: On the transfer of energy in stationary mountain waves. *Geofys. Publ.*, **22,** 1–23.

Gage, K. S., and W. H. Reid, 1968: The stability of thermally stratified plane Poiseuille flow. *J. Fluid Mech.*, **33,** 21–32.

Gill, A. E., 1982: *Atmosphere-Ocean Dynamics.* Academic Press, 662 pp.

Hauf, T., and T. L. Clark, 1989: Three-dimensional numerical experiments on convectively forced internal gravity waves. *Quart. J. Roy. Meteor. Soc.*, **115,** 309–333.

Hazel, P., 1972: Numerical studies of the stability of inviscid stratified shear flows. *J. Fluid Mech.*, **51,** 39–61.

Hebert, D., J. N. Moum, C. A. Paulson, D. R. Caldwell, T. K. Chereskin, and M. J. McPhaden, 1991: The role of the turbulent stress divergence in the equatorial Pacific zonal momentum balance. *J. Geophys. Res.*, **96,** 7127–7136.

——, ——, ——, and ——, 1992: Turbulence and internal waves at the equator. Part II: Details of a single event. *J. Phys. Oceanogr.*, **22,** 1346–1356.

Jones, J. H., 1973: Vertical mixing in the equatorial undercurrent. *J. Phys. Oceanogr.*, **3,** 286–295.

Klemp, J. B., and R. B. Wilhelmson, 1978: The simulation of three-dimensional convective storm dynamics. *J. Atmos. Sci.*, **35,** 1070–1096.

——, and D. R. Durran, 1983: An upper boundary condition permitting internal gravity wave radiation in numerical mesoscale models. *Mon. Wea. Rev.*, **111,** 430–445.

Kuettner, J. P., P. A. Hildebrand, and T. P. Clark, 1987: Convection waves: Observations of gravity wave systems over convectively active boundary layers. *Quart. J. Roy. Meteor. Soc.*, **113,** 445–467.

Lilly, D. K., 1962: On the numerical simulation of buoyant convection. *Tellus,* **14,** 148–171.

Lindzen, R. S., and J. W. Barker, 1985: Instability and wave over-reflection in stably stratified shear flow. *J. Fluid Mech.*, **151,** 189–217.

McPhaden, M. J., and B. A. Taft, 1988: Dynamics of seasonal and intraseasonal variability in the eastern equatorial Pacific. *J. Phys. Oceanogr.*, **18,** 1713–1732.

——, and H. Peters, 1992: On the diurnal cycle of internal wave variability in the equatorial Pacific Ocean: Results from moored observations. *J. Phys. Oceanogr.*, **22,** 1317–1329.

Moeng, C.-H., 1984: A large-eddy-simulation model for the study of planetary boundary-layer turbulence. *J. Atmos. Sci.*, **41,** 2052–2062.

Moore, D. W., and S. G. H. Philander, 1978: Modelling of the tropical ocean circulation. *The Sea,* Vol. 6, Wiley-Interscience, 319–361.

Moum, J. N., D. R. Caldwell, and C. A. Paulson, 1989: Mixing in the equatorial surface layer and thermocline. *J. Geophys. Res.*, **94,** 2005–2021.

——, D. Hebert, C. A. Paulson, and D. R. Caldwell, 1992: Turbulence and internal waves at the equator. Part I. Statistics from towed thermistors and a microstructure profiler. *J. Phys. Oceanogr.*, **22,** 1330–1345.

Peters, H., M. C. Gregg, and J. M. Toole, 1988: On the parameterization of equatorial turbulence. *J. Geophys. Res.*, **93,** 1199–1218.

Rosenthal, A. J., and R. S. Lindzen, 1983: Instabilities in a stratified fluid having one critical level. Part I: Results. *J. Atmos. Sci.*, **40,** 509–520.

Smagorinsky, J., 1963: General circulation experiments with primitive equations. I: The basic experiment. *Mon. Wea. Rev.*, **91,** 99–164.

Smith, R. B., 1979: The influence of mountains on the atmosphere. *Advances in Geophysics,* Vol. 21, Academic Press, 87–230.

Turner, J. S., 1973: *Buoyancy Effects in Fluids.* Cambridge University Press, 92–94.

UNESCO, 1981: Tenth Report on the Joint Panel of Oceanographic Tables and Standards (1981). UNESCO Tech. Papers in Mar. Sci., No. 30, p. 24.

van Leer, B., 1977: Towards the ultimate conservative difference scheme. IV: A new approach to numerical convection. *J. Comput. Phys.*, **23,** 276–299.

Wijesekera, H. W., and T. M. Dillon, 1991: Internal waves and mixing in the upper equatorial Pacific Ocean. *J. Geophys. Res.*, **96,** 7115–7126.

Winters, K. B., and E. A. D'Asaro, 1989: Two-dimensional instability of finite amplitude internal gravity wave packets near a critical level. *J. Geophys. Res.*, **94,** 12 709–12 719.

——, and J. J. Riley, 1992: Instability of internal waves near a critical level. *Atmos.-Ocean,* **16,** 249–278.